Effect of dynamic plastic deformation on the microstructure and mechanical properties of an Al-Zn-Mg alloy

Mohamed A. Afifi[a,b], Ying Chun Wang[a,c*] ,Terence G. Langdon[d]

[a]School of Materials Science and Engineering, Beijing Institute of Technology, Beijing 100081, China

[b]Brunel Centre for Advanced Solidification Technology (BCAST), Brunel University London, Uxbridge UB8 3PH, UK

[c]National Key Laboratory of Science and Technology on Materials under Shock and Impact, Beijing 100081, China

[d]Materials Research Group, Department of Mechanical Engineering, University of Southampton, Southampton SO17 1BJ, UK

*Corresponding author: Ying Chun Wang, e-mail: wangyc@bit.edu.cn

Abstract

A supersaturated Al-Zn-Mg alloy was processed by dynamic plastic deformation (DPD) using a Split-Hopkinson pressure bar (SHPB) facility with strain range from 0.5 to 1.5 and then subjected to compressive testing at strain rates of 1×10^{-3} ~ 4×10^{3} s^{-1}. The results show that there is concurrent occurrence of grain refinement, increase in dislocation density and precipitation of fine precipitates in different morphologies during DPD at strain over 1. This enhances the yield strength of the Al alloy after DPD over the as-received material in peak-aging state (T6). Grains are refined through the formation of low angle grain boundaries (LAGBs) by rearrangement of dislocations which leads to the subdivision of original grains. Heterogeneous coarse precipitates mainly of T ($Al_{20}Cu_2Mn_3$) and E ($Al_{18}Mg_3Cr_2$) phases distribute along dislocations and grain boundaries after DPD. Dynamic precipitation of very fine η' and η during DPD occurs where the volume fraction of precipitates increases with increasing the number of presses. The influence of precipitates on the strain rate sensitivity is also discussed.

Keywords: Al-Zn-Mg alloy; dynamic plastic deformation; precipitates; split-Hopkinson pressure bar; strain rate sensitivity

1. Introduction

Dynamic plastic deformation (DPD) is an attractive technique providing the capability of achieving grain refinement after deformation at strain rates of the order of 10^2-10^3 s^{-1} [1-5]. Many different DPD processing methods have been developed including Split Hopkinson Pressure Bar (SHPB) or high-speed hammer impacting [6,7], Dynamic Channel Angular Pressing (DCAP) [8] and Dynamic High-Pressure Torsion (DHPT) [9]. Within these methods, SHPB impacting is an especially effective way for producing ultrafine-grained (UFG) materials through the multi-axial impact of rectangular samples or by the unidirectional impact of cylindrical samples at a high strain rate of ~10^3 s^{-1} for several presses [6].

Several reports are now available describing the evolution of microstructure and the underlying mechanical properties of aluminium (Al) and Al-based alloys after dynamic testing [10-16]. For example, it was shown that dynamic compression of a peak-aged Al-Zn-Mg alloy at 4.0×10^3 s^{-1} assists the precipitation process through precipitate coalescence [16]. Very recent experiments demonstrated that DHPT processing of pure Al enhanced the dislocation density and led to the formation of a finer cell structure leading to an improvement in hardness up to strains of ~ 2.5 [17]. Another study found that after one DCAP pass in 3003 and 5556 Al alloys the average grain size decreased to less than ~0.5 μm with the presence of a high density of dislocations and an increase in hardness [18]. Thus, the grains are refined and this is assisted by dynamic recrystallization after increasing numbers of DCAP passes up to 4 [18]. In another related study, the microstructure of an Al-Cu-Mg alloy subjected to dynamic compression was primarily of dynamic recrystallized grains and dislocation accumulation led to an improved yield strength [19]. Accordingly, it is concluded that the processing of Al alloys by DPD can refine the grains, increase the dislocation density and produce enhanced mechanical properties.

Aluminium alloys are widely used in aerospace, automobile, and other structural applications due to their high strength-to-weight ratio and good fracture toughness [20-23]. In practice, they may be subjected to dynamic shock loading during service. For example, the striking of miscellaneous objects on armaments, the occurrence of flying bodies on landing and automotive driving collisions are cases in which the mechanical components experience high strain rate loadings [24]. Furthermore, understanding the material behaviour during deformation under different strain rates is of major importance for further developing these engineering applications [25]. There is also great interest in using Al alloys in aerospace applications, as in wing and fuselage structures, where these parts may be subjected to loading at different strain rates [21, 26-27]. In addition, the effect of precipitate evolution in plastically-deformed Al-Zn-Mg alloys on the mechanical properties at different strain rates has been rarely studied [28] and more investigations are required to understand the influence of microstructure on the strain rate dependence of the mechanical properties.

A review shows that only limited data are available to date documenting the microstructural response and the mechanical behaviour of Al-Zn-Mg alloys at different strain rates after DPD processing for different strains. Accordingly, and in order to address this deficiency, the present investigation was initiated to examine the microstructural evolution and the mechanical behaviour of an Al-Zn-Mg alloy under quassi-static compression (1.0×10^{-3} s^{-1}) and under high strain rates (2.0×10^{3} s^{-1} and 4.0×10^{3} s^{-1}) after processing by DPD using the SHPB procedure.

2. Experimental material and procedures

The investigated Al-Zn-Mg alloy has a chemical composition (wt.%) of Al-4.53 Zn-2.52 Mg-0.35 Mn-0.2 Cr-0.11 Cu-0.1 Zr received as a plate in a T6 state (solid solution treatment at 743 K for 1 h and peak aging at 393 K for 24 h). The material was cut into cylinders with diameters of 14 mm and lengths of 18 mm and then were heated to an homogenization

temperature of 853 K and quenched in water followed by a solid solution (SS) treatment at 743 K for 1 h and again quenched in water before DPD. The cylinders were subjected to DPD at a strain rate of ~10^3 s^{-1} under uniaxial compression at room temperature (RT, ~298 K) using an SHPB facility as described earlier [29] with input and output bars having diameters of 30 mm. The Al alloy was pressed for 2, 4 and 6 times to reach strains of ~0.5, ~1.0 and ~1.5 where the strain was estimated as $\ln(L_0/L_f)$, where L_0 and L_f are the cylinder heights before and after the DPD processing, respectively. This processing combining a solid solution heat treatment and DPD processing is henceforth designated SS-DPD.

Cylindrical compression specimens with 5 mm in diameter and 4 mm in height were cut from the as-received and the centres of the DPD-processed cylinders. Quasi-static compression testing was performed at room temperature under a strain rate of 1.0×10^{-3} s^{-1} using an Instron testing machine. Dynamic testing at strain rates of 2.0×10^3 and 4.0×10^3 s^{-1} were conducted using SHPB with input and output bars having diameters of 10 mm. The microstructures of the as-received and the SS-DPD processed alloy were characterized by Electron Backscatter Diffraction (EBSD) analysis by a scanning electron microscope (SEM) FEI Quanta 650F. The average grain size was measured from the grain boundary spacing determined using the linear intercept method. Low-angle grain boundaries (LAGBs) were defined as having misorientation differences from 2° to 15° and high-angle grain boundaries (HAGBs) had misorientations larger than 15°. Microstructures were observed also using transmission electron microscopy (TEM) with an F20 Field Emission TEM equipped with a scanning unit and an energy dispersive (EDS) detector operating at 200 kV. The TEM samples were prepared by electro-polishing as described earlier [30]. The average particle sizes were evaluated through calculating the mean of ~500 particles for each condition [31]. The foil thickness measurements were performed for quantifying the volume fraction of precipitates using convergent beam electron diffraction (CBED). The TEM region was tilted

to collect a two-beam condition with a dark Kikuchi line crossing the $(000)_{Al}$ bright disk and a bright Kikuchi line crossing the $(220)_{Al}$ dark disk in the CBED. A full detailed description of the thickness determination is given elsewhere [32].

3. Experimental results

3.1 Mechanical behaviour at different strain rates

The true stress-true strain curves of the as-received and the SS-DPD processed alloy are shown in Fig. 1 for strain rates of (a) 1.0×10^{-3}, (b) 2.0×10^{3} and (c) 4.0×10^{3} s^{-1}. It is apparent that the yield strength increases with increasing numbers of DPD presses and DPD processing for over 4 presses enhances the yield strength under both quasi-static and dynamic testing by comparison with the as-received alloy in the T6 state. Thus, the yield strengths at 1.0×10^{-3} s^{-1} after 4 and 6 presses are ~410 and ~450 MPa which are higher than the as-received material by ~14% and ~22%, respectively. Similarly, they are higher by ~14% and ~25% at 2.0×10^{3} s^{-1} and by ~8% and ~11% at 4.0×10^{3} s^{-1} than for the as-received condition tested at identical strain rates. However, the yield strengths of the Al alloy processed by DPD for 2 presses are lower than for the as-received alloy at all three stain rates. In addition, Fig.1 shows the as-received alloy has a higher peak stress by comparison with the SS-DPD processed Al alloys due to its superior work hardening capability.

It is evident that the yield strength increases with increasing strain rate from 1.0×10^{-3} to 4.0×10^{3} s^{-1}. The incremental increase in yield strength for the as-received alloy is ~20 MPa from 1.0×10^{-3} to 2.0×10^{3} s^{-1} and ~70 MPa from 2.0×10^{3} to 4.0×10^{3} s^{-1} while the increments are ~30 and ~120 MPa for the 2 presses of SS-DPD, ~30 and ~110 MPa for 4 presses of SS-DPD and ~30 and ~100 MPa for 6 presses of SS-DPD with increasing strain rates from 1.0×10^{-3} to 2.0×10^{3} and 4.0×10^{3} s^{-1}, respectively. Thus, it is concluded that there is a minor increase in the yield strength with increasing strain rate from 1.0×10^{-3} to 2.0

$\times 10^3$ s^{-1} in the as-received and the SS-DPD processed samples but a major increase when the strain rate is increased from 2.0×10^3 to 4.0×10^3 s^{-1}.

3.2. Microstructure characterization after DPD

Typical EBSD orientation maps of the as-received and the SS-DPD processed alloy are shown in Fig. 2 where these maps were recorded on the transverse sections perpendicular to the compression direction. Inspection of Fig. 2(a) shows that the as-received alloy has mainly an elongated structure with HAGBs and some evolved equiaxed grains with average sizes of ~1.3 μm. After 2 presses of SS-DPD the microstructure is again elongated but the grains are refined to ~1 μm as shown in Fig. 2(b). Increasing the numbers of presses to 4 leads to some coarse elongated grains transforming to equiaxed subgrains having fine LAGBs together with the presence of a few recrystallized grains as denoted by arrows in Fig. 2(c). A further increase to 6 presses and most elongated structures disappear so that more fine equiaxed grains are present with LAGBs as depicted by arrows in Fig. 2(d). The average grain sizes determined by EBSD after 4 and 6 presses were ~0.8 and ~0.7 μm, respectively.

The misorientation angles for the as-received and the SS-DPD processed Al alloy are shown in Fig.3. It is apparent from Fig. 3(a) that the as-received alloy has a high fraction of LAGBs (~64%) and this fraction further increases after DPD to 78% and 86% when increasing from 2 to 6 presses as depicted in Figs 3(b-d). The increase in the LAGBs is due to the formation of more subgrains at higher DPD strains [33].

The corresponding $\{111\}_{Al}$ pole figures for the as-received Al alloy and after DPD pressing are presented in Fig. 4. In Fig. 4(a) it is apparent that the texture in the as-received alloy is an annealing texture $\{110\}\langle 001\rangle_{Al}$ and a shear texture $\{100\}\langle 011\rangle_{Al}$ with a peak intensity of 4.29 MUD (multiple of uniform density) [34]. There is a strong texture of intensity 12.94 MUD after DPD processing for 2 presses where a cube texture $\{100\}\langle 001\rangle_{Al}$ is dominant as in Fig. 4(b) but this texture is transformed to shear $\{100\}\langle 011\rangle_{Al}$ in the DPD

processed Al alloys for 4 and 6 presses as in Figs. 4(c,d). The texture intensity is also high after 4 presses by 11.9 MUD and further increases to 15.37 after 6 presses which is attributed to the recrystallization during deformation [33].

Typical TEM micrographs of the supersaturated Al alloy followed by DPD processing are shown in Fig. 5. Inspection of Fig. 5(a) shows the microstructure after 2 presses of DPD has elongated grains containing dislocation tangles. The visible precipitates occurring primarily along grain boundaries and dislocations as displayed in Fig. 5(b) are spherical with diameters of ~40 nm or plate-like with average lengths of ~60 nm. The estimated volume fractions were ~0.05$\pm$0.004 for the spherical and ~0.03$\pm$0.004 for the platelets, respectively. Indexing along $<110>_{Al}$ showed the precipitates are G.P. zones along $1/3\{220\}_{Al}$, η' along $\{100\}_{Al}$, η along $\{111\}_{Al}$, T ($Al_{20}Cu_2Mn_3$) along $\{123\}_{Al}$ and E ($Al_{18}Mg_3Cr_2$) phase along $\{133\}_{Al}$ [35-37].

Fig. 5(c) shows grains and subgrains having high dislocation density after DPD for 4 presses. The precipitates are mainly of η' along $\{100\}_{Al}$, η along $\{111\}_{Al}$, T phase along $\{123\}_{Al}$ and E phase along$\{331\}_{Al}$ as depicted in Fig. 5(d). The size of the spherical precipitates slightly decreases after 4 presses to ~35 nm and the platelet particles have average length of ~40 nm. The volume fraction of precipitates also increases after 4 presses to ~0.055$\pm$0.003 for the spherical and ~0.04$\pm$0.002 for the platelets, respectively.

After DPD processing for 6 presses, the elongated grains are replaced with some fine new grains which contains dislocation networks within the grains as shown in Fig. 5(e). The selected area electron diffraction (SAED) pattern in Fig. 5(f) shows that the precipitates are predominantly η' across $\{112\}_{Al}$, η at $\{113\}_{Al}$ with diffraction spots of T phase along $\{032\}_{Al}$ and E phase along $\{113\}_{Al}$. The average size of the spherical precipitates after 6 presses is ~30 nm and the platelet average lengths are ~40 nm with increased volume fractions to ~0.07$\pm$0.003 for the spherical and ~0.04$\pm$0.003 for the platelet precipitates, respectively.

Grain boundary precipitates (GBP) with spherical and platelet morphologies are observed along the grain boundaries as denoted by arrows in Figs. 5(b,d,f). It is clear that increasing the number of DPD presses leads to an increase in the number of precipitates across the GB. The dislocation densities were estimated by XRD and the values were ~2.5 × 10^{13}, ~2.85 × 10^{14}, ~3.0 × 10^{14} and ~3.1 × 10^{14} m^{-2} in the as-received and the SS-DPD processed alloys after 2, 4 and 6 presses, respectively.

Fine G.P. zones and η precipitates were observed in the HRTEM micrographs and the corresponding fast Fourier transform (FFT) pattern presented in Fig. 6 after DPD for 2 presses [38]. Thus, Fig. 6(a) shows coarse T and E precipitates along dislocation tangles and at a higher magnification in Fig. 6(b) it is clear that the T and E phases are incoherent with the Al matrix which is consistent with earlier results [30].

The overlapping of precipitates and the presence of fine η' and η precipitates are displayed in a series of TEM micrographs of the DPD sample after 4 presses in Fig. 7. Fig. 7(a) shows coarse particles on dislocations with the presence of twinning within these particles and Fig. 7(b) displays selected fine η' and η precipitates with size ranges of ~5 nm as identified by the FFT pattern. An η phase is observed attached to the T phase presented in the high resolution transmission electron microscopy (HRTEM) image of Fig. 7(c) where the η phase is identified through the FFT pattern along $\{111\}_{Al}$. The inverse FFT pattern shows incoherency between the two phases along the $\{111\}_{Al}$ plane. Another fine η phase close to dislocations along $\{111\}_{Al}$ is attached to the T phase where the interface has three twinning planes along $\{022\}_{Al}$ as depicted in the HRTEM image and corresponding FFT pattern in Fig. 7(d). Dislocations close to the precipitates lead to lattice distortions in the interfaces between the precipitates and the Al matrix which transform these dislocations into twins during severe straining [30, 39]. Fig. 8 shows TEM micrographs of the Al-Zn-Mg alloy processed by SS-DPD for 6 presses. Coarse precipitates are present along the dislocations and grain boundaries

as shown in Fig. 8(a). HRTEM observations show the presence of fine platelet η precipitates having lengths of ~12 nm across $\{011\}_{Al}$ as depicted in Fig. 8(b). Fig. 8(c) shows a HRTEM image of other fine η precipitates along dislocations with diameters of ~15 nm. A selected E phase shows the presence of multiple twinning with the aid of HRTEM in Fig. 8(d) identified by the FFT pattern along $\{400\}_{Al}$.

4. Discussion

41 The mechanism of grain refinement during DPD

Observations of the Al alloy processed by DPD at ~10^3 s^{-1} through EBSD and TEM show the occurrence of dynamic recrystallization. The Al alloy has a high stacking fault energy so that at the start of plastic deformation the multiple slip system promotes a dense dislocation wall formation on the slip planes [40]. LAGBs form subgrains by the rearrangement of dislocations [41] and therefore the initial stages of straining introduce high dislocation densities which rearrange in cellular substructures with further strain. This leads to a subdivision of the original grains into much more heavily misoriented small areas. The boundaries around these small areas are the so-called incidental boundaries which are essentially low-angle boundaries consisting of stored dislocations [42, 43]. Inspection of Fig. 2 shows that the as-received material grains are elongated. During SS-DPD processing, the elongated grains after 2 SS-DPD presses start to evolve into finer grains with LAGBs at a DPD strain of 0.5 and these have a strong texture as presented in Fig. 4. Then with further dynamic deformation a series of recrystallized grains with LAGBs start to form within these primitive elongated grains.

4.2 Precipitate evolution during DPD

In the present investigation, heterogeneous coarse precipitates were observed across the dislocations and grain boundaries after DPD processing. These precipitates were mainly of spherical and platelet morphologies with some overlapping of T and E phases while η' and η

precipitates were very fine as verified by the HRTEM images where the volume fraction of precipitates increased with increasing numbers of presses as shown in Fig. 5.

It is suggested that the fine precipitates, mainly of G.P. zones, η' and η, observed in the DPD processed Al alloy shown in Figs. 6, 7 and 8 through HRTEM images are dynamically formed during deformation [44, 45]. Thus, the G.P. zones are nucleated by displacement of very small numbers of solute atoms during the waiting time of dislocations when they are pinned by solute obstacles [44]. The growth of the precipitates and the transformation of G.P. zones into more stable phases are assisted by pipe diffusion along the dislocation lines during further straining [38, 44]. The coarse T and E phases observed after 2 DPD presses may be present during the homogenization treatment before DPD processing [46, 47]. In practice, the presence of coarse T and E phases close to dislocations is attributed to the atomic movement generated by dislocation slip which can induce significant solute diffusion during compression at high strain rates [48]. GBP are observed after DPD processing and this increases with increasing numbers of DPD presses. This is due to the lower free energy barrier for precipitate nucleation along the boundaries by comparison with the matrix [49]. In addition, both solute segregation and solute diffusion along the boundaries increase the rate of providing solute atoms for nucleation [49].

The density of mobile dislocations also plays an important role in the precipitate evolution during DPD. The T and E phases after 6 presses of DPD are sheared by the increased dislocation density and the nucleation of fine precipitates is assisted by dislocation motion leading to a reduction in the precipitates average size. Inspection of Fig. 5 shows that the amount of platelet precipitates decreases while spherical precipitates increase in size after increasing the numbers of presses from 4 to 6. The coarse platelet precipitates are sheared by dislocations with further straining and they are fragmented into spherical morphologies which continue to increase in size after 6 presses through rapid solutes diffusion assisted by

dislocations [50]. The presence of η located at the edges of the T phase can be attributed to the decomposition of the T phase during the deformation. Similar observations were also reported in Al-Cu and Al-Mg binary alloys showing a dissolution of precipitates under severe deformation conditions [51-53].

4.3 The strengthening after DPD processing

The results of the compression tests show that SS-DPD processing for 4 and 6 presses are beneficial in improving the yield strength compared to the as-received Al-Zn-Mg alloy in the T6 state. The first contribution to an increase in the yield strength of the DPD samples is solid solution strengthening. The strengthening effect of solutes in the Al-Zn-Mg alloy may be estimated from the relationship [54]:

$$\sigma_{ss} = \sigma_{Zn} + \sigma_{Mg} = B_{Zn} c_{Zn}^{2/3} + B_{Mg} c_{Mg}^{2/3} \qquad (1)$$

where σ_{Zn} and σ_{Mg} are the effective strengthening components related to the Zn and Mg solutes, respectively, B_{Zn} and B_{Mg} are constants related to the size, modulus and electronic mismatch of the solutes including various resolution factors and having values of 3.1 and 20.5, respectively [55] and c_{Zn} and c_{Mg} are the solute concentrations in wt% of the Al alloy processed by SS-DPD. Thus, solute strengthening by Mn, Cr, Cu and Zr are ignored as the content of these solutes are all generally less than 0.5 wt.% in the Al-Zn-Mg alloy [55]. If all solute atoms are assumed to be within the matrix, the solid solution strengthening is estimated as ~50 MPa. However, the solute atom concentration in the DPD-processed alloy is much less than in the solid solution because precipitates form by dynamic precipitation and consume many of the solute atoms within the matrix during the DPD processing. Thus, it is concluded that solid solution strengthening provides a small contribution to the overall strengthening of the DPD samples.

It was shown from Figs 2 and 5 that DPD processing for 4 and 6 presses leads to grain refinement. However, the microstructure after DPD pressing mainly consists of a deformed

structure where the majority boundaries are LAGBs. Thus, the Hall-Petch relationship is not applicable for grain boundary strengthening and strengthening by grains consists mainly of a cellular dislocation structure through the relationship [56]

$$\sigma_{GB} = \frac{nGb}{d} \qquad (2)$$

where n is a constant of the order of ~10, G is the shear modulus, b is the Burgers vector and d is the average grain size. It is apparent that grain refinement to ~0.8 μm and ~0.7 μm through SS-DPD for 4 and 6 presses contributes to an increase of strength compared to the as-received material having grains with an average size of ~1.3 μm.

The precipitates enhance the strength of the SS-DPD-processed Al alloy by either dislocation shearing and/or the Orowan dislocation bypassing mechanisms [57-59]. Precipitation strengthening increases with an increasing volume fraction of fine precipitates [60]. Moreover, increasing the numbers of SS-DPD presses leads to an increase in the dislocation density as shown in Fig.5 and this leads to enhancing the yield strength according to the Bailey–Hirsch relationship [61]. In addition, strengthening by dislocations is greater in the deformed materials than in the as-received sample as it requires a higher stress to activate alternative dislocation sources [62]. Thus the combination of grain refinement, the increase in the dislocation density and the volume fraction of the precipitates after 4 and 6 presses of SS-DPD all contribute to the improved strength of the material over the as-received Al alloy [30].

The strength after SS-DPD for 2 presses is lower than for the as-received material despite of the increase in the dislocation density after the SS-DPD presses. This is owing to the lower numbers of fine precipitates due to an insufficient dynamic precipitation as presented in Fig. 5(b) compared with the as-received alloy from peak aging as demonstrated in earlier work [30].

The Al alloy subjected to DPD processing has a lower work hardening rate than the as-received alloy. This is a consequence of the DPD-processed alloy containing a higher density

of dislocations as shown in Fig.5 which leads to the occurrence of dynamic recovery during compression and thereby assists in decreasing the work hardening rate by comparison with the as-received alloy [63, 64].

4.4 Effect of strain rate on compressive strength after DPD

Fig. 1 shows that the yield strengths of the as-received and the SS-DPD-processed alloy increase with increasing strain rate. The strain rate sensitivity exponent (SRS), *m*, can be expressed as follows [65]:

$$m = \frac{\log(\sigma_2/\sigma_1)}{\log(\dot{\varepsilon}_2/\dot{\varepsilon}_1)} \qquad (3)$$

where σ_1 and σ_2 are the yield strengths at strain rates of $\dot{\varepsilon}_1$ and $\dot{\varepsilon}_2$, respectively.

Fig. 9 displays the variation of the yield strength with strain rate. Although there is an increase by ~20~30 MPa in yield strength for all experimental samples with increasing strain rates from 1.0×10^{-3} to 2.0×10^{3} s^{-1}, the SRS is essentially insensitive to the numbers of DPD presses. The SRS may be expressed with respect to the solute diffusion coefficient, *D*, and the dislocation waiting time, t_w, through the expression [66]:

$$m = \frac{\sqrt{3}k_bT}{b^2 \times l}[1-(K(Dt_w)^{2/3}] \qquad (4)$$

where k_b is Boltzmann's constant, *T* is the absolute temperature, *l* is the dislocation spacing and *K* is a factor dependent upon the dislocation motion and solute-dislocation binding energy [28]. According to Eq. (4), the formation of precipitates assisted by dynamic precipitation after DPD pressing causes an increase in the dislocation waiting time by pinning the dislocations and decreasing the dislocation spacing, thereby leading to a reduction in the values of *m*. At the same time, the values of *m* tend to increase assisted by grain refinement after DPD and compensating the reduced values from the pinning of dislocations by precipitates. This maintains $m \approx 0.006$ for different numbers of DPD presses [66, 67].

Dislocation motion is mainly controlled by thermal activation within the low strain rate regime and by a drag mechanism in the high strain rate regime [68, 69]. Under low strain rates for $\dot{\varepsilon} \ll 1$, the increase in strength is given by [70]:

$$\sigma = \sigma_0(1 - e^{-k_1\dot{\varepsilon}}C_2(T)) \quad (5)$$

where σ_0 is a reference flow stress, k_1 is a material constant and $C_2(T)$ is a factor depending on temperature which is also a constant in the current work. The increase in strength in the high strain rate regime (2×10^3 to 4×10^3 s^{-1}) can be expressed as [70]:

$$\sigma = \sigma_0 e^{c_1\dot{\varepsilon}} \quad (6)$$

where c_1 is a material constant and $\dot{\varepsilon}$ is the strain rate. From Eqs. (5-6), the rise in strength is greater with increasing strain rates from 2×10^3 to 4×10^3 s^{-1} by comparison with the values upon increasing strain rate from 1×10^{-3} to 2×10^3 s^{-1}. Following Eq. (3), the value of m with increasing strain rate from 2×10^3 to 4×10^3 s^{-1} is higher than with increasing strain rate from 1×10^{-3} to 2×10^3 s^{-1} as verified in Fig. 9 and this result is similar to the strain rate dependence of strength in the same alloy after ECAP [66].

In addition, for increasing strain rates from 2×10^3 to 4×10^3 s^{-1} the SRS shows a decrease with the DPD presses increasing from 2 to 6. This is attributed to the impeding effect of the higher dislocation density with increasing DPD pressing to the mobility of dislocations [71].

5. Summary and conclusions

1. Experiments on an Al-Zn-Mg solid solution alloy show that the high dislocation densities produced from high straining during DPD pressing rearrange to form cellular substructures and fine grains having LAGBs with a strong shear texture.

2. Precipitates of fine η' and η are dynamically formed during DPD processing in the Al alloy. Coarse T and E phases are formed either in the vicinity of dislocations or across grain

boundaries. Mobile dislocations assist in the nucleation and growth of precipitates which can further lead to a coalescence of precipitates. Precipitates are sheared by dislocations during straining and fragmented to form spherical morphologies.

3. DPD pressing for 4 and 6 presses after a solid solution treatment enhances the yield strength over the peak-aged alloy under compression tests at different strain rates. This is attributed to a combination of grain refinement, an increased dislocation density and the large numbers of fine precipitates produced by the DPD processing.

4. Increasing the strain rate from 1×10^{-3} to 2×10^{3} s^{-1}, the SRS value is maintained constant with increasing numbers of presses because the reduction in SRS from the pinning of dislocations by more precipitates is compensated by the increased SRS assisted by grain refinement after DPD. The SRS from 2.0×10^{3} to 4.0×10^{3} s^{-1} decreases with increasing numbers of DPD presses caused by an increase in the dislocation density and a decrease in the mobility of dislocations. The SRS is higher with a strain rate increase from 2.0×10^{3} to 4.0×10^{3} s^{-1} than from 1.0×10^{-3} to 2.0×10^{3} s^{-1} due to dislocation motion through different mechanisms.

Acknowledgements

This work was supported in part by the National Natural Science Foundation of China under Grant no. 51671030 and in part by the European Research Council under ERC Grant Agreement no. 267464-SPDMETALS.

Data Availability

The raw/processed data required to reproduce these findings cannot be shared at this time as the data also forms part of an ongoing study.

References

[1] P. R. Rao, S. V. Kamat and G. Sundararajan, Material deformation and fracture under impulsive loading conditions, Bull. Mater. Sci. 15 (1992) 3–25. doi: 10.1007/BF02745213.

[2] Z.P. Luo, H.W. Zhang, N. Hansen, K. Lu, Quantification of the microstructures of high purity nickel subjected to dynamic plastic deformation, Acta Mater. 60 (2012) 1322–1333. doi:10.1016/j.actamat.2011.11.035.

[3] Z.P. Luo, O. V. Mishin, Y.B. Zhang, H.W. Zhang, K. Lu, Microstructural characterization of nickel subjected to dynamic plastic deformation, Scr. Mater. 66 (2012) 335–338. doi:10.1016/j.scriptamat.2011.11.022.

[4] Y.S. Li, N.R. Tao, K. Lu, Microstructural evolution and nanostructure formation in copper during dynamic plastic deformation at cryogenic temperatures, Acta Mater. 56 (2008) 230–241. doi:10.1016/j.actamat.2007.09.020.

[5] C.S. Hong, N.R. Tao, X. Huang, K. Lu, Nucleation and thickening of shear bands in nano-scale twin/matrix lamellae of a Cu–Al alloy processed by dynamic plastic deformation, Acta Mater. 58 (2010) 3103–3116. doi:10.1016/j.actamat.2010.01.049.

[6] Y. Yang, Y. Chen, F. Ma, H. Hu, Q. Zhang, T. Tang, X. Zhang, Microstructure Evolution of 1050 Commercial Purity Aluminum Processed by High–Strain–Rate Deformation, J. Mater. Eng. Perform. 24 (2015) 4307–4312. doi:10.1007/s11665-015-1769-6.

[7] L. Farbaniec, A. Abdul–Latif, J. Gubicza, G. Dirras, High purity ultrafine–grained nickel processed by dynamic plastic deformation: Microstructure and mechanical properties, Adv. Eng. Mater. 14 (2012) 1027–1033. doi:10.1002/adem.201200034.

[8] J.H. Han, J.Y. Suh, K.K. Jee, J.C. Lee, Evaluation of formability and planar anisotropy based on textures in aluminum alloys processed by a shear deforming process, Mater. Sci. Eng. A. 477 (2008) 107–120. doi:10.1016/j.msea.2007.04.117.

[9] H. Lanjewar, L. Kestens, P. Verleysen, Dynamic High Pressure Torsion (DHPT) – A Novel Method for High Strain Rate Severe Plastic Deformation, Proceedings (18th Intl. Conf. on Exptl Mechanics) 2 (2018) 1–7. doi:10.3390/icem18-05399.

[10] L. Zhen, G.A. Li, J.S. Zhou, D.Z. Yang, Micro–damage behaviors of Al–6Mg alloy impacted by projectiles with velocities of 1–3.2 km/s, Mater. Sci. Eng. A. 391 (2005) 354–366, doi:10.1016/j.msea.2004.09.016.

[11] R. Kapoor, J.B. Singh, J.K. Chakravartty, High strain rate behavior of ultrafine–grained Al–1.5 Mg, Mater. Sci. Eng. A. 496 (2008) 308–315. doi:10.1016/j.msea.2008.05.043.

[12] B. Mishra, C. Mondal, R. Goyal, P. Ghosal, K.S. Kumar, V. Madhu, Plastic flow behavior of 7017 and 7055 aluminum alloys under different high strain rate test methods, Mater. Sci. Eng. A. 612 (2014) 343–353. doi:10.1016/ j.msea.2014.06.037.

[13] W.S. Lee, Z.C. Tang, Relationship between mechanical properties and microstructural response of 6061–T6 aluminum alloy impacted at elevated temperatures, Mater. Des. 58 (2014) 116–124. doi:10.1016/j.matdes.2014.01.053.

[14] E. El–Magd, M. Brodmann, Influence of precipitates on ductile fracture of aluminium alloy AA7075 at high strain rates, Mater. Sci. Eng. A. 307 (2001) 143–150. doi:10.1016/S0921-5093(00)01961-4.

[15] K.O. Pedersen, T. Børvik, O.S. Hopperstad, Fracture mechanisms of aluminium alloy AA7075–T651 under various loading conditions, Mater. Des. 32 (2011) 97–107. doi:10.1016/j.matdes.2010.06.029.

[16] M.A. Afifi, P.H.R. Pereira, Y.C. Wang, Y. Wang, S. Li, T.G. Langdon, Effect of ECAP processing on microstructure evolution and dynamic compressive behavior at different temperatures in an Al–Zn–Mg alloy, Mater. Sci. Eng. A. 684 (2017) 617–625. doi:10.1016/j.msea.2016.12.099.

[17] P. Verleysen, H. Lanjewar, Dynamic high pressure torsion: A novel technique for dynamic severe plastic deformation, J. Mater. Process. Technol. 276 (2020) 1–11. doi:10.1016/j.jmatprotec.2019.116393.

[18] I.G. Brodova, I.G. Shirinkina, O.A. Antonova, E. V. Shorokhov, I.I. Zhgilev, Formation of a submicrocrystalline structure upon dynamic deformation of aluminum alloys, Mater. Sci. Eng. A. 503 (2009) 103–105. doi:10.1016/j.msea.2007.12.060.

[19] A.A. Tiamiyu, R. Basu, A.G. Odeshi, J.A. Szpunar, Plastic deformation in relation to microstructure and texture evolution in AA 2017–T451 and AA 2624–T351 aluminum alloys under dynamic impact loading, Mater. Sci. Eng. A. 636 (2015) 379–388. doi:10.1016/j.msea.2015.03.113.

[20] M.E. Fine, Precipitation hardening of aluminum alloys, Metall. Trans. A 6 (1975) 625–630. doi:10.1007/BF02672283.

[21] T. Dursun, C. Soutis, Recent developments in advanced aircraft aluminium alloys, Mater. Des. 56 (2014) 862–871. doi:10.1016/j.matdes.2013.12.002.

[22] A.A.D. Sarhan, E. Zalnezhad, M. Hamdi, The influence of higher surface hardness on fretting fatigue life of hard anodized aerospace AL7075–T6 alloy, Mater. Sci. Eng. A. 560 (2013) 377–387. doi:10.1016/j.msea.2012.09.082.

[23] Y.C. Wang, M. A.Afifi, X. Cheng, S. Li, T.G. Langdon, An evaluation of the microstructure and microhardness in an Al–Zn–Mg alloy processed by ECAP and post-ECAP heat treatments, Adv. Eng. Mater. 22 (2020) 1901040(1-8). DOI: 10.1002/adem.201901040.

[24] F.F. Saniee, S.S. Boroujeni, S. Lahmi, G.H. Majzoobi, An Experimental Investigation on the Strain Rate Sensitivity of a Severely Deformed Aluminum Alloy, Exp. Mech. 55 (2015) 569–576. doi:10.1007/s11340-014-9968-x.

[25] J. R. Klepaczko, C. Y. Chiem, On rate sensitivity of f.c.c. metals, instantaneous rate sensitivity and rate sensitivity of strain hardening, J. Mech. Phys. Solids 34 (1986) 29–54. doi: 10.1016/0022-5096(86)90004-9.

[26] D. Varas, J. L.–Puente, R. Zaera, Experimental analysis of fluid–filled aluminium tubes subjected to high–velocity impact, Int. J. Imp. Eng. 36 (2009) 81–91. doi:10.1016/j.ijimpeng.2008.04.006.

[27] B. Egan, C.T. McCarthy, M.A. McCarthy, P.J. Gray, R.M. O'Higgins, Static and high–rate loading of single and multi–bolt carbon–epoxy aircraft fuselage joints, Compos. Part A. 53 (2013) 97–108. doi:10.1016/j.compositesa.2013.05.006.

[28] S. Zhang, W. Hu, R. Berghammer, G. Gottstein, Microstructure evolution and deformation behavior of ultrafine–grained Al–Zn–Mg alloys with fine η' precipitates, Acta Mater. 58 (2010) 6695–6705, doi:10.1016/j.actamat.2010.08.034.

[29] L. Wang, Y.C. Wang, A.P. Zhilyaev, A.V. Korznikov, S. Li, E. Korznikova, T.G. Langdon, Dynamic compressive behavior of ultrafine–grained pure Ti at elevated temperatures after processing by ECAP, J. Mater. Sci. 49 (2014) 6640–6647. doi: 10.1007/s10853-014-8306-0.

[30] M.A. Afifi, Y.C. Wang, P.H.R. Pereira, Y. Wang, S. Li, Y. Huang, T.G. Langdon, Characterization of precipitates in an Al–Zn–Mg alloy processed by ECAP and subsequent annealing, Mater. Sci. Eng. A. 712 (2018) 146–156. doi:10.1016/j.msea.2017.11.091.

[31] M.T. Shehata, Practical Guide to Image Analysis, ASM International, Materials Park, OH, 2000, pp. 129–143.

[32] David B. Williams, C. Barry Carter, Transmission Electron Microscopy A Textbook for Materials Science, Springer, New York, 2009.

[33] P.H.R. Pereira, Y.C. Wang, Y. Huang, T.G. Langdon, Influence of grain size on the flow properties of an Al–Mg–Sc alloy over seven orders of magnitude of strain rate, Mater. Sci. Eng. A. 685 (2017) 367–376. doi:10.1016/j.msea.2017.01.020.

[34] J. Li, F. Li, X. Ma, J. Li, S. Liang, L. Zhang, Effects of Heat Treatment on Microstructure and Mechanical Properties of an ECAPed Al–Zn–Mg–Cu Alloy, Adv. Eng. Mater. 20 (2018) 1–10. doi:10.1002/adem.201701155.

[35] G. Sha, A. Cerezo, Early–stage precipitation in Al–Zn–Mg–Cu alloy (7050), Acta Mater. 52 (2004) 4503–4516. doi:10.1016/j.actamat.2004.06.025.

[36] A. Kverneland, V. Hansen, R. Vincent, K. Gjønnes, J. Gjønnes, Structure analysis of embedded nano–sized particles by precession electron diffraction. η'–precipitate in an Al–Zn–Mg alloy as example, Ultramicroscopy 106 (2006) 492–502. doi:10.1016/j.ultramic.2006.01.009.

[37] W.B. Pearson, A Handbook of Lattice Spacings and Structures of Metals and Alloys, Pergamon Press, Oxford, 1958.

[38] T. Hu, K. Ma, T.D. Topping, J.M. Schoenung, E.J. Lavernia, Precipitation phenomena in an ultrafine–grained Al alloy, Acta Mater. 61 (2013) 2163–2178. doi:10.1016/j.actamat.2012.12.037.

[39] K. Ogawa, Edge dislocations dissociated in {112} planes and twinning mechanism of b.c.c. metals, Philos. Mag. 11 (1965) 217–233. doi: 10.1080/14786436508221852.

[40] J. P. Hirth, J. Lothe, Theory of Dislocations, second ed., Wiley, New York, 1982.

[41] R. Kaibyshev, O.Sitdikov, I. Mazurina, D.R. Lesuer, Deformation behavior of a 2219 Al alloy, Mat. Sci. Eng. A 334 (2002) 104–113. doi: 10.1016/S0921-5093(01)01777-4.

[42] D.K. Wilsdorf, N. Hansen, Geometrically necessary, incidental and subgrain boundaries, Scr. Metall. Mater. 25 (1991) 1557–1562. doi: 10.1016/0956-716X(91)90451-6.

[43] G. Winther, X. Huang, A. Godfrey, N. Hansen, Critical comparison of dislocation boundary alignment studied by TEM and EBSD: technical issues and theoretical consequences, Acta Mater. 52 (2004) 4437–4446. doi:10.1016/j.actamat.2004.05.050.

[44] A. Deschamps, M. Niewczas, F. Bley, Y. Brechet, J. D. Embury, L. Le Sinq, F. Livet, J. P. Simon, Low–temperature dynamic precipitation in a supersaturated A–Zn–Mg alloy and related strain hardening, Phil. Mag. A79 (1999) 2485–2504. doi:10.1080/01418619908214295.

[45] G. Waterloo, V. Hansen, J. Gjønnes, S.R. Skjervold, Effect of predeformation and preaging at room temperature in Al – Zn – Mg – (Cu, Zr) alloys, Mat. Sci. Eng. A 303 (2001) 226–233. doi: 10.1016/S0921-5093(00)01883-9.

[46] L. Lodgaard, N. Ryum, Precipitation of dispersoids containing Mn and/or Cr in Al–Mg–Si alloys, Mater. Sci. Eng. A 283 (2000) 144–152. doi:10.1016/S0921-5093(00)00734-6.

[47] Y.R. Zhou, L. Kang, C.H. Duan, G. Zhao, N. Tian, Control of dispersolds in 7475 aluminum alloy, Mater. Sci. Forum 941 (2018) 896–901. doi:10.4028/www.scientific.net/MSF.941.896.

[48] A. Deschamps, F.Bley, F.Livet, D.Fabregue, L.David, In–situ Small–Angle X–ray Scattering study of dynamic precipitation in an Al–Zn–Mg–Cu alloy, Phil. Mag. 83 (2003) 677–692. doi: 10.1080/0141861021000051091.

[49] J. Bernardini, P. Gas, E.D. Hondros, M.P. Seah, The role of Solute Segregation in grain boundary diffusion, Proc. R. Soc. A 379 (1982) 159–178. doi:10.1098/rspa.1982.0011.

[50] H.J. Roven, M. Liu, J.C. Werenskiold, Dynamic precipitation during severe plastic deformation of an Al–Mg–Si aluminium alloy, Mater. Sci. Eng. A. 483–484 (2008) 54–58. doi:10.1016/j.msea.2006.09.142.

[51] W. Huang, Z. Liu, M. Lin, X. Zhou, L. Zhao, A. Ning, S. Zeng, Reprecipitation behavior in Al–Cu binary alloy after severe plastic deformation–induced dissolution of θ' particles, Mater. Sci. Eng. A. 546 (2012) 26–33. doi:10.1016/j.msea.2012.03.010.

[52] Z. Liu, S. Bai, X. Zhou, Y. Gu, On strain–induced dissolution of θ' and θ particles in Al–Cu binary alloy during equal channel angular pressing, Mater. Sci. Eng. A. 528 (2011) 2217–2222. doi:10.1016/j.msea.2010.12.060.

[53] M.A. Muñoz-Morris, C. G. Oca, D.G. Morris, Mechanical behaviour of dilute Al–Mg alloy processed by equal channel angular pressing, Scr. Mater. 48 (2003) 213–218. doi:10.1016/S1359-6462(02)00501-8.

[54] H.R. Shercliff, M.F. Ashby, a process model for age hardening of aluminium alloys– I. the model, Acta. Metall. Mat. 38 (1990) 1789–1802. doi: 10.1016/0956-7151(90)90291-N.

[55] M. Dixit, R.S. Mishra, K.K. Sankaran, Structure–property correlations in Al 7050 and Al 7055 high–strength aluminum alloys, Mater. Sci. Eng. A. 478 (2008) 163–172. doi: 10.1016/j.msea.2007.05.116.

[56] H. Mughrabi, Plastic deformation and fracture of materials. In: High-Temperature Deformation and Creep of Crystalline Solids, Wiley–VCH, Weinheim, Germany, 1993, 373.

[57] A.J. Ardell, Precipitation hardening, Metall. Trans. A. 16 (1985) 2131–2165. doi:10.1007/BF02670416.

[58] C.B. Fuller, D.N. Seidman, D.C. Dunand, Mechanical properties of Al (Sc, Zr) alloys at ambient and elevated temperatures, Acta Mater. 51 (2003) 4803–4814. doi:10.1016/S1359-6454(03)00320-3.

[59] K. Ma, H. Wen, T. Hu, T.D. Topping, D. Isheim, D.N. Seidman, E.J. Lavernia, J.M. Schoenung, Mechanical behavior and strengthening mechanisms in ultrafine grain

precipitation–strengthened aluminum alloy, Acta Mater. 62 (2014) 141–155. doi:10.1016/j.actamat.2013.09.042.

[60] M.A. Afifi, Y.C. Wang, P.H.R. Pereira, Y. Huang, Y. Wang, X. Cheng, S. Li, T.G. Langdon, Mechanical properties of an Al–Zn–Mg alloy processed by ECAP and heat treatments, J. Alloys Compd. 769 (2018) 631–639. doi:10.1016/j.jallcom.2018.07.343.

[61] J.E. Bailey, P.B. Hirsch, The dislocation distribution, flow stress, and stored energy in cold–worked polycrystalline silver, Philos. Mag. 5 (1960) 485–497. doi:10.1080/14786436008238300.

[62] X. Huang, N. Hansen, N. Tsuji, Hardening by Annealing and Softening by Deformation in Nanostructured Metals, Science 312 (2006) 249–251. doi:10.1126/science.1124268.

[63] N.Y. Zolotorevsky, A.N. Solonin, A.Y. Churyumov, V.S. Zolotorevsky, Study of work hardening of quenched and naturally aged Al–Mg and Al–Cu alloys, Mater. Sci. Eng. A. 502 (2009) 111–117. doi:10.1016/j.msea.2008.10.010.

[64] D. Chu, J.W. Morris, The influence of microstructure on work hardening in aluminum, Acta Mater. 44 (1996) 2599–2610. doi:10.1016/1359-6454(95)00403-3.

[65] J. May, H.W. Höppel, M. Göken, Strain rate sensitivity of ultrafine–grained aluminium processed by severe plastic deformation, Scr. Mater. 53 (2005) 189–194. doi:10.1016/j.scriptamat.2005.03.043.

[66] M. A. Afifi, Y.C. Wang, X. Cheng, S. Li, T. G. Langdon, Strain rate dependence of compressive behavior in an Al–Zn–Mg alloy processed by ECAP, J. Alloys Compd., 791 (2019) 1079–1087. doi: 10.1016/j.jallcom.2019.03.390.

[67] S. Zhang, Y.C. Wang, A.P. Zhilyaev, E. Korznikova, S. Li, G.I. Raab, T.G. Langdon, Effect of grain size on compressive behaviour of titanium at different strain rates, Mater. Sci. Eng. A. 645 (2015) 311–317. doi:10.1016/j.msea.2015.08.031.

[68] G. Regazzoni, U.F. Kocks, P.S. Follansbee, Dislocation kinetics at high strain rates, Acta Metall. 35 (1987) 2865–2875. doi:10.1016/0001-6160(87)90285-9.

[69] A. Kumar, F.E. Hauser, J.E. Dorn, Viscous drag on dislocations in Aluminum at high Strain Rates, Acta Metall. 16 (1968) 1189–1197. doi:10.1016/0001-6160(68)90054-0.

[70] A.S. Khan, H. Liu, Variable strain rate sensitivity in an aluminum alloy: Response and constitutive modeling, Int. J. Plast. 36 (2012) 1–14. doi:10.1016/j.ijplas.2012.02.001.

[71] P.J. Worthington, B.J. Brindley, Serrated yielding in substitutional alloys, Philos. Mag. 19 (1969) 1175–1178. doi:10.1080/14786436908228642.

Figure Captions

Fig.1 True stress-true strain curves of the as-received and the SS-DPD processed Al-Zn-Mg alloy at strain rates of (a) 1.0×10^{-3}, (b) 2.0×10^{3} and (c) 4.0×10^{3} s^{-1}.

Fig. 2 EBSD orientation colour maps of (a) the as-received and the SS-DPD processed alloy for (b) 2, (c) 4 and (d) 6 presses.

Fig. 3 Histogram of the misorientation angle distributions for (a) the as-received and the SS-DPD processed alloy for (b) 2, (c) 4 and (d) 6 presses.

Fig. 4 Texture represented as {111} pole figures of (a) the as-received and the SS-DPD processed alloy for (b) 2, (c) 4 and (d) 6 presses.

Fig. 5 Typical TEM micrographs of Al-Zn-Mg alloy after SS-DPD processing for (a) 2 presses, (b) 2 presses at higher magnification with corresponding SAED along $<110>_{Al}$, (c) 4 presses, (d) 4 presses at higher magnification with corresponding SAED along $<110>_{Al}$, (e) 6 presses and (f) 6 presses at higher magnification with corresponding SAED along $<110>_{Al}$.

Fig. 6 TEM micrographs of the Al-Zn-Mg alloy processed by SS-DPD for 2 presses showing: (a) coarse precipitation across dislocations and (b) HRTEM image of T and E phases.

Fig. 7 Micrographs of the Al-Zn-Mg alloy processed by SS-DPD for 4 presses showing: (a) coarse precipitates along dislocation tangles with presence of twinning within dislocations, (b) HRTEM image of very fine η' and η precipitates, (c) HRTEM image showing an η phases formation attached with the T phase and (d) HRTEM of an η phase attached with the T phase through triple twinning.

Fig. 8 Micrographs of the Al-Zn-Mg alloy processed by SS-DPD for 6 presses showing: (a) coarse precipitates across dislocations and grain boundaries, (b) fine η precipitates along dislocations (c) HRTEM of a selected fine η and (d) HRTEM of an E phase with presence of multiple twinning.

Fig. 9 Logarithmic plot of stress at yield point against strain rate at 1.0×10^{-3}, 2.0×10^{3} and 4.0×10^{3} s^{-1} for the SS-DPD processed Al alloy.

Figure(s)

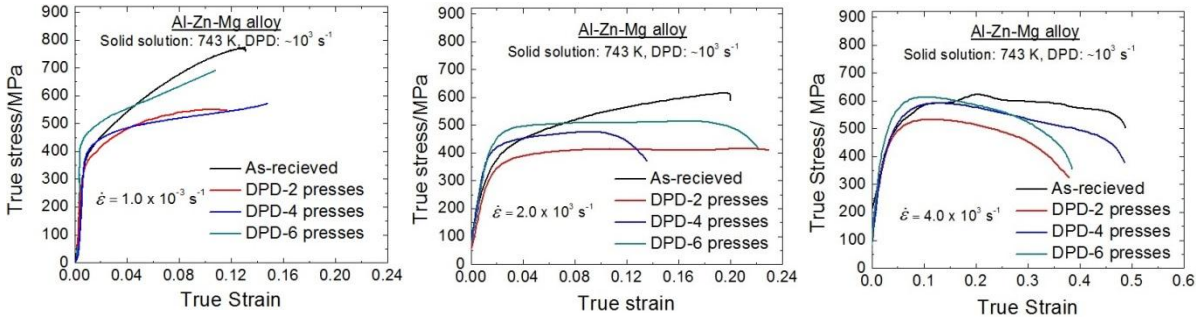

(a) (b) (c)

Fig.1 True stress-true strain curves of the as-received and the SS-DPD processed Al-Zn-Mg alloy at strain rates of (a) 1.0×10^{-3}, (b) 2.0×10^{3} and (c) 4.0×10^{3} s^{-1}.

Figure(s)

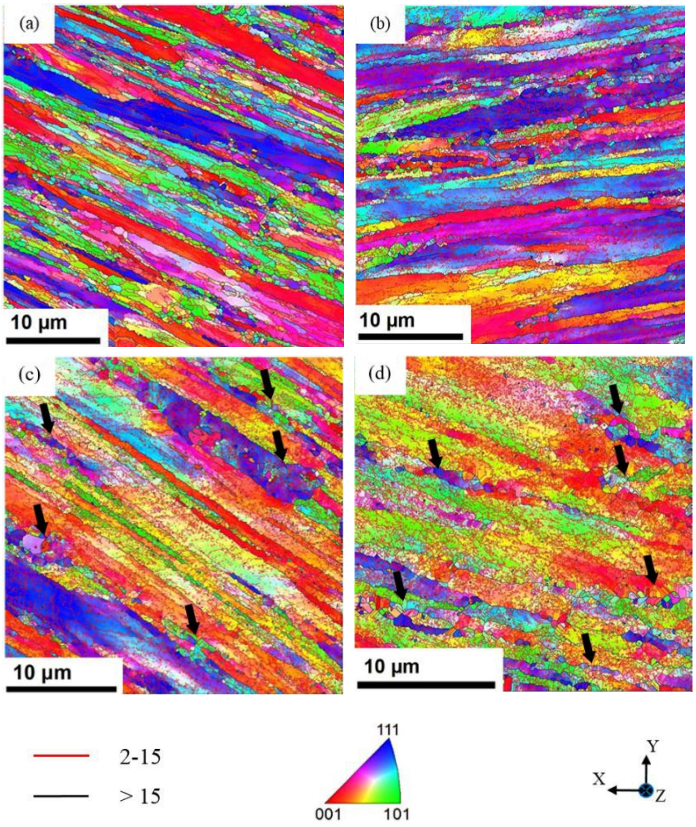

Fig. 2 EBSD orientation colour maps of (a) the as-received and the SS-DPD processed alloy for (b) 2, (c) 4 and (d) 6 presses.

Figure(s)

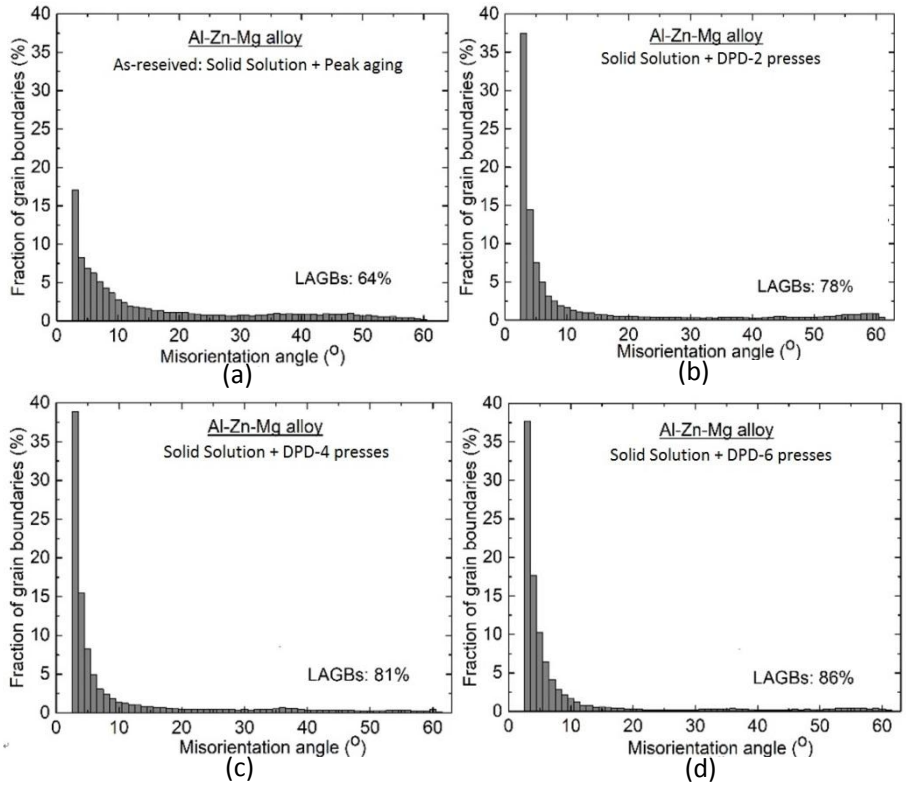

Fig. 3 Histogram of the misorientation angle distributions for (a) the as-received and the SS-DPD processed alloy for (b) 2, (c) 4 and (d) 6 presses.

Figure(s)

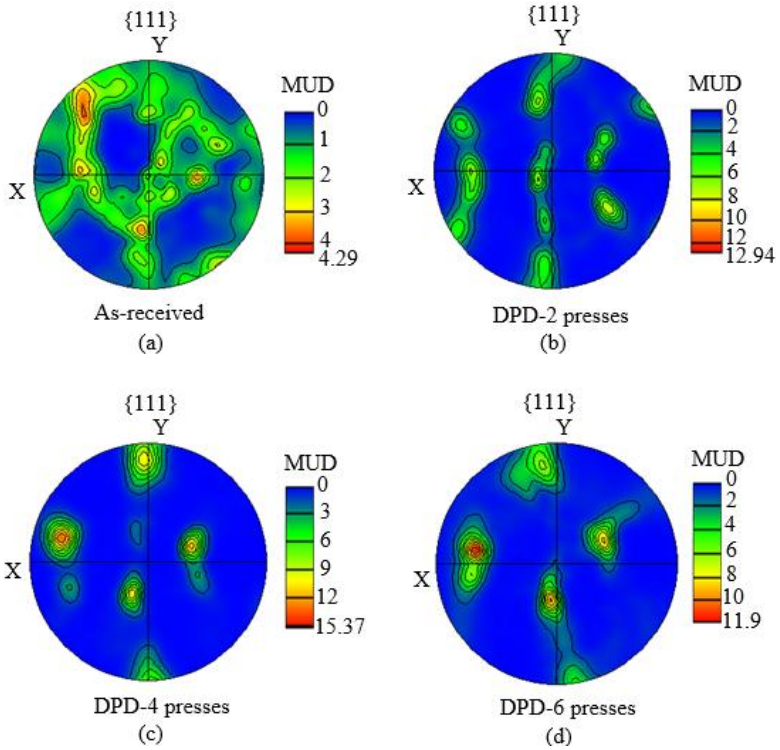

Fig. 4 Texture represented as {111} pole figures of (a) the as-received and the SS-DPD processed alloy for (b) 2, (c) 4 and (d) 6 presses.

Figure(s)

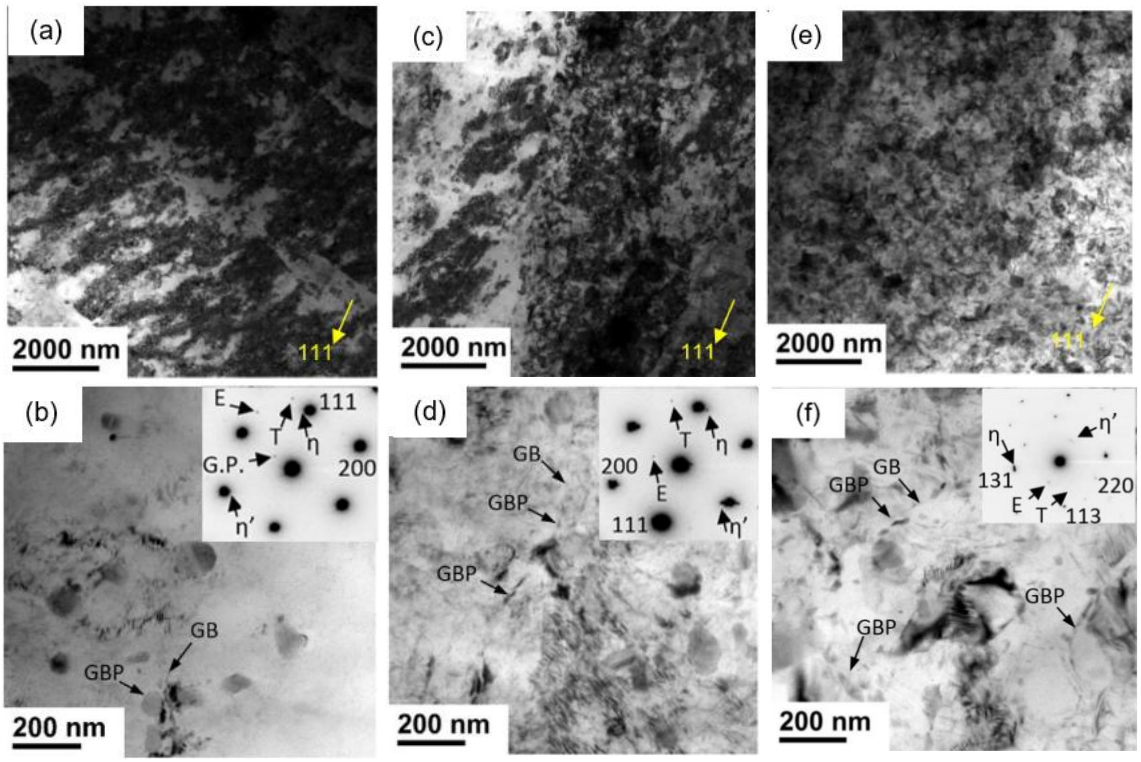

Fig. 5 Typical TEM micrographs of Al-Zn-Mg alloy after SS-DPD processing for (a) 2 presses, (b) 2 presses at higher magnification with corresponding SAED along $<110>_{Al}$, (c) 4 presses, (d) 4 presses at higher magnification with corresponding SAED along $<110>_{Al}$, (e) 6 presses and (f) 6 presses at higher magnification with corresponding SAED along $<110>_{Al}$.

Figure(s)

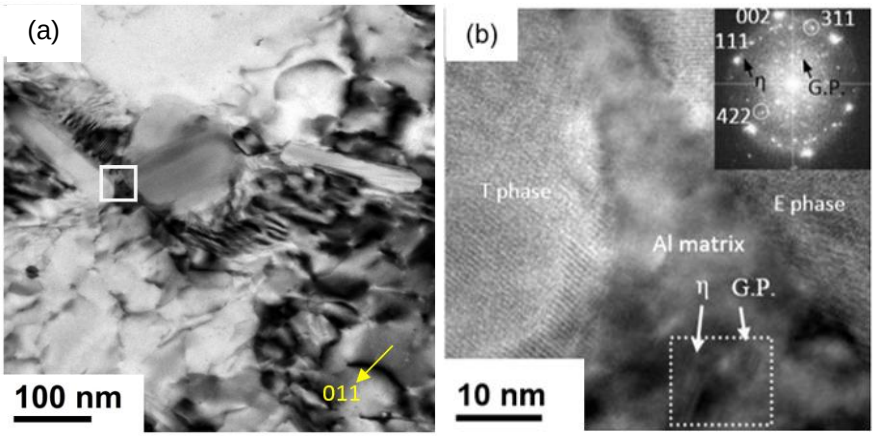

Fig. 6 TEM micrographs of the Al-Zn-Mg alloy processed by SS-DPD for 2 presses showing: (a) coarse precipitation across dislocations and (b) HRTEM image of T and E phases.

Figure(s)

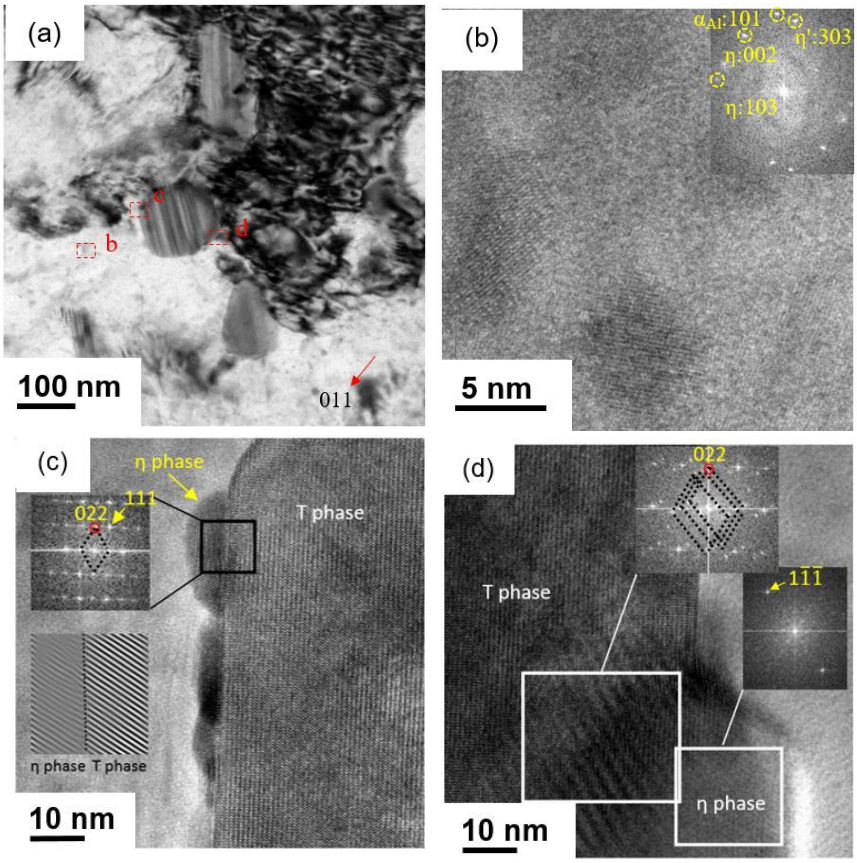

Fig. 7 Micrographs of the Al-Zn-Mg alloy processed by SS-DPD for 4 presses showing: (a) coarse precipitates along dislocation tangles with presence of twinning within dislocations, (b) HRTEM image of very fine η' and η precipitates, (c) HRTEM image showing an η phases formation attached with the T phase and (d) HRTEM of an η phase attached with the T phase through triple twinning.

Figure(s)

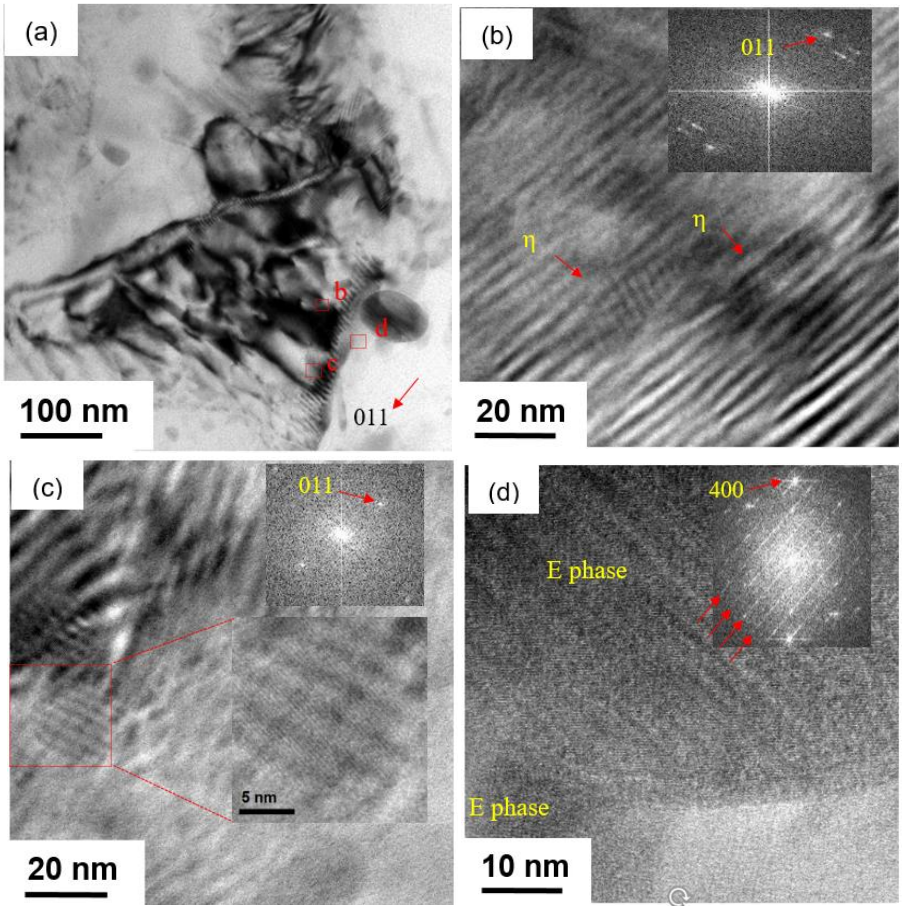

Fig. 8 Micrographs of the Al-Zn-Mg alloy processed by SS-DPD for 6 presses showing: (a) coarse precipitates across dislocations and grain boundaries, (b) fine η precipitates along dislocations (c) HRTEM of a selected fine η and (d) HRTEM of an E phase with presence of multiple twinning.

Figure(s)

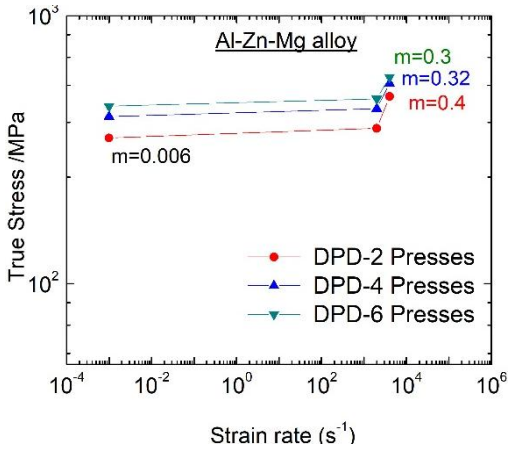

Fig. 9 Logarithmic plot of stress at yield point against strain rate at 1.0×10^{-3}, 2.0×10^{3} and 4.0×10^{3} s^{-1} for the SS-DPD processed Al alloy.